Constraining Data Mining with Physical Models: Voltage- and Oxygen Pressure-Dependent Transport in Multiferroic Nanostructures

5 AUTHORS, INCLUDING:

Alexei Belianinov
Oak Ridge National Laboratory
37 PUBLICATIONS **89** CITATIONS

SEE PROFILE

Sergei V Kalinin
Oak Ridge National Laboratory
626 PUBLICATIONS **11,121** CITATIONS

SEE PROFILE

Constraining Data Mining with Physical Models: Voltage- and Oxygen Pressure-Dependent Transport in Multiferroic Nanostructures

Evgheni Strelcov,[†] Alexei Belianinov,[†] Ying-Hui Hsieh,[‡] Ying-Hao Chu,[‡,§] and Sergei V. Kalinin*[,†]

[†]Institute for Functional Imaging of Materials and Center for Nanophase Materials Sciences, Oak Ridge National Laboratory, Oak Ridge, Tennessee 37831, United States

[‡]Department of Materials Science and Engineering, National Chiao Tung University, Hsinchu 30010, Taiwan

[§]Institute of Physics, Academia Sinica, Taipei 105, Taiwan

Ⓢ *Supporting Information*

ABSTRACT: Development of new generation electronic devices necessitates understanding and controlling the electronic transport in ferroic, magnetic, and optical materials, which is hampered by two factors. First, the complications of working at the nanoscale, where interfaces, grain boundaries, defects, and so forth, dictate the macroscopic characteristics. Second, the convolution of the response signals stemming from the fact that several physical processes may be activated simultaneously. Here, we present a method of solving these challenges via a combination of atomic force microscopy and data mining analysis techniques. Rational selection of the latter allows application of physical constraints and enables direct interpretation of the statistically significant behaviors in the framework of the chosen physical model, thus distilling physical meaning out of raw data. We demonstrate our approach with an example of deconvolution of complex transport behavior in a bismuth ferrite−cobalt ferrite nanocomposite in ambient and ultrahigh vacuum environments. Measured signal is apportioned into four electronic transport patterns, showing different dependence on partial oxygen and water vapor pressure. These patterns are described in terms of Ohmic conductance and Schottky emission models in the light of surface electrochemistry. Furthermore, deep data analysis allows extraction of local dopant concentrations and barrier heights empowering our understanding of the underlying dynamic mechanisms of resistive switching.

KEYWORDS: *Bismuth ferrite, cobalt ferrite, oxide heterostructures, multivariate analysis, Bayesian linear unmixing, FORC-IV*
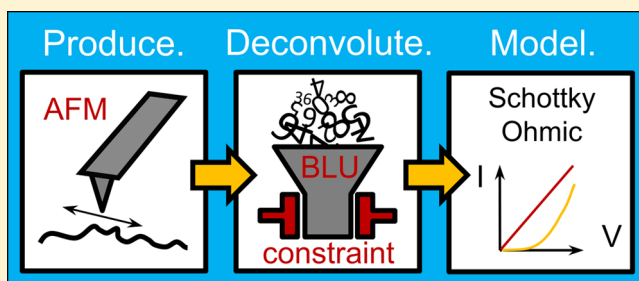
A complex interplay of physics and chemistry in transition metal oxides determines their electronic, magnetic, optical, and ferroic properties enabling a wide range of applications of these materials.[1−5] It is well understood that the macroscopic characteristics are often governed by micro- and nanoscopic elements: interfaces, grain boundaries, defects, and dislocations. Exploration of these features led to recent discoveries of 2D electron gas in oxide heterointerfaces,[6,7] grain boundary and ferroelectric domain wall conduction,[8−14] and polarization-controlled tunneling in ferroelectric films.[15−18] Further progress in these studies is hampered by the nanoscopic nature of the studied objects and their highly convoluted response to external excitations. For instance, electronic transport can be strongly influenced by lattice or field-controlled metal−insulator transitions,[19−21] synchronous voltage-activated electrochemical processes,[22−26] gas adsorption,[27,28] or ferroelectric polarization switching.[15,29,30]

In recent decades, the nanoscale obstacle has been addressed by development of advanced scanning probe microscopy (SPM) techniques.[31−35] However, the deconvolution of mechanisms remains a challenge; in fact, strong confinement of electric field in the tip−surface junction often enables transport mechanisms absent in relatively low uniform fields of macroscopic measurements. A promising pathway to decouple physical responses has been to employ multivariate statistical methods to unmix complex behaviors from multidimensional response data sets.[36−38] It is crucially important to select data mining methods compatible with researcher-imposed physical constraints in order to interpret statistically significant traits in the data in terms of relevant physical models.

Recently, we have shown that Bayesian Linear Unmixing (BLU) algorithm[39] can be used to separate intricate electron transport in the $BiFeO_3$−$CoFe_2O_4$ (BFO−CFO) nanocomposite into four well-behaved components with clear physical meaning, described by specific transport models.[40] This is possible since BLU was equipped with the sum-to-one and
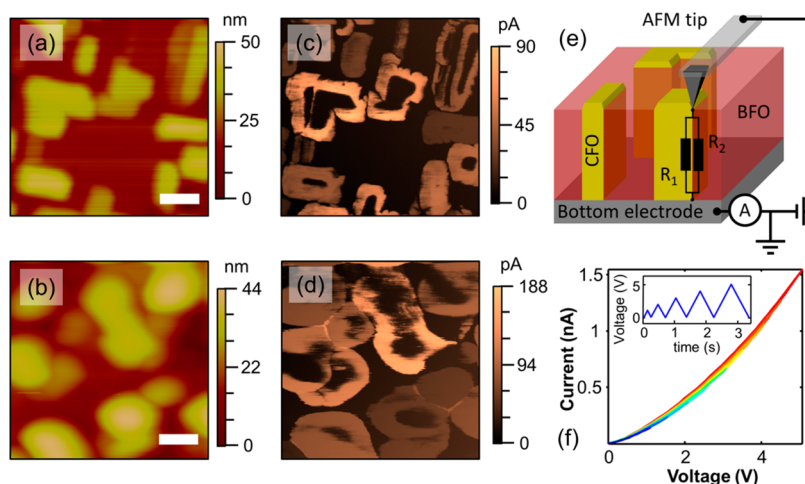
Figure 1. BFO−CFO nanocomposite. (a,b) Typical topographic AFM images of the BFO−CFO nanocomposite recorded in ambient and UHV conditions, respectively. (c,d) Corresponding current maps at tip bias of 0.1 V. Note how the AFM tip sharpness affected the clarity of the topo images and width of the conductive interface. (e) A schematic of the FORC-IV setup; R1 and R2 are modeling resistances of the two constituent materials. (f) FORC-IV curves averaged over a 50×50 spatial grid (2500 curves total) as measured in ambient over a region of 500×500 nm^2; inset shows the used FORC voltage waveform with five triangular pulses.

non-negativity constraints. Here, we restrict BLU with another physically important constraint and perform in-depth analysis of the dependence of the conductive components on voltage and ambient oxygen and water pressure. We postulate that introduction of physical constraints into the statistical models will open the pathway for systematic deep data studies of physical functionalities on the nanoscale via scanning probe microscopy and other local probing techniques.

BFO−CFO nanocomposite is an interesting complex oxide system that has attracted much attention due to its ferroelectric, ferromagnetic, and magnetoelectric properties as a promising platform for the new-generation multiferroic memory and logic devices.[41−43] It has also been reported that this material can possess very unusual transport properties,[42,44] presumably dependent on the growth conditions.[43] The complex conductive behavior, manifested by the heterogeneous tubular interface of BFO−CFO nanocomposite, can only be understood through a thorough and sophisticated analysis. We utilize a combination of FORC-IV technique[45,46] and deep data analysis as applied in two measurement conditions: ambient and ultrahigh vacuum (UHV). This allows us to probe conductive phenomena with high resolution in both spatial and energy (voltage) domains at the extremes of partial oxygen and water pressure and thus to shed light onto the mechanisms thereof. We focus our discussion on the analysis of four FORC-IV data sets of the BFO−CFO sample recorded in both ambient and UHV with the maximal peak bias of the voltage waveforms (V_p) at 3 and 5 V. As suggested earlier,[40] conductivity at the tubular interface might be controlled by oxygen vacancies and thus should be sensitive to oxygen partial pressure. On the other hand, variation in relative air humidity from 0% to 87% also alters transport behaviors,[47] showing sensitivity of the conduction mechanisms to water vapor partial pressure.

Results and Discussion. At a very low AFM tip bias (e.g., 0.1 V) and ambient conditions (298 K room temperature, relative humidity ca. 40%), the BFO−CFO interfaces have 2−3 orders of magnitude higher conductivity than the constituent oxides (Figure 1a−c). Placing the sample in UHV (base pressure 1×10^{-10} Torr or better) followed by surface cleaning

by light outgassing at 50 °C overnight has increased the interfacial current about 2-fold but left the BFO matrix and CFO pillars cores as insulating as before (Figure 1b−d). In order to investigate the transport behavior with a better voltage resolution and tap into different transport regimes, we used FORC waveforms comprised of several triangular pulses, such as shown in the inset of Figure 1f; the waveforms have peak biases of 1, 2, 3, 4, and 5 V. The voltage waveforms were applied to the sample via AFM tip sequentially at each pixel of a 50×50 grid overlaid on a spatial region of 500×500 nm^2. Current was read off of the bottom electrode (see schematics of Figure 1e). As the tip polarity in the present work is always positive, no ferroelectric switching occurs in the BFO matrix and thus control over the interfacial conductivity is leveraged not by polarization (as in ref 44) but by other mechanisms discussed below. The response averaged over the whole grid (2500 individual FORC-IV curves) is presented in Figure 1f for an ambient data set. Averaging is equivalent to a lossy compression of the original data set in which the information on the spatial distribution of conductive behavior is lost. On the other hand, the original data set is four-dimensional ($I = f(x, y, V, V_p)$) and cannot be easily visualized or comprehended, thus necessitating application of an analytical tool capable of lossless compression into a set of 2D objects amenable to perception by the researcher. Multivariate statistical techniques such as principal component analysis (PCA), independent component analysis (ICA), k-means clustering, and so forth are examples of such tools, that can transform a multidimensional data set into an array of 2D loading maps conveying spatial information and 1D eigenvectors, preserving spectral information. However, these methods are purely statistical and therefore not constrained by any physical models, producing statistically significant results that are difficult to interpret physically. In the case of PCA and ICA, both eigenvectors and loading maps can have negative values or display other types of unphysical behavior. Therefore, as shown previously,[40] we chose BLU as a tool for analysis of the FORC-IV data. This method, developed[48] by the Dobigeon group, endeavors to solve a blind unmixing problem by presenting the data in a $Y = MA + N$ form, where the complete observations Y, are a linear
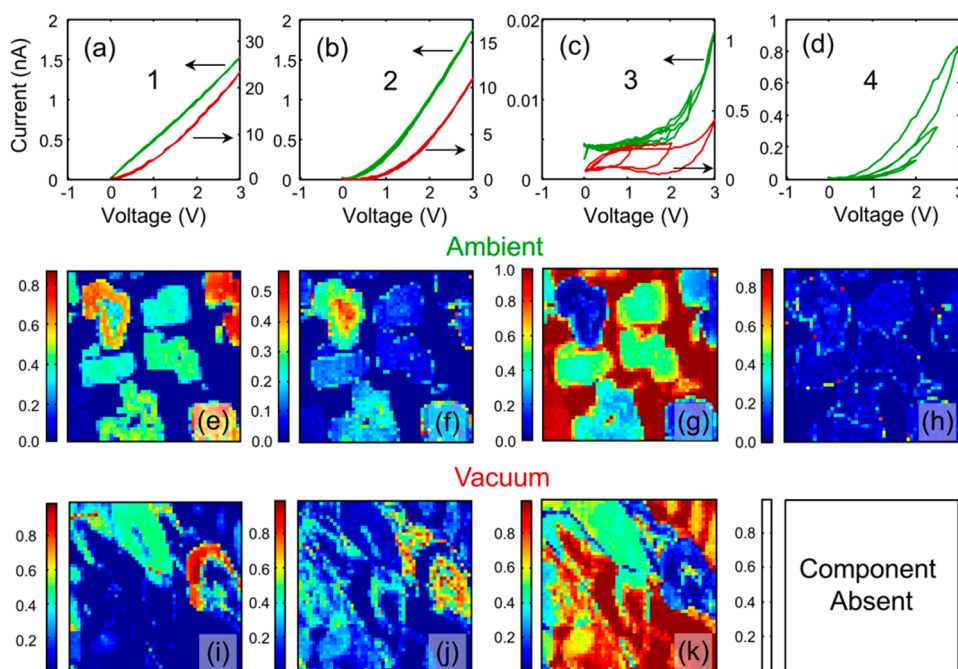
Figure 2. BLU of the FORC-IV data sets with maximal V_p = 3 V. (a−d: Bayesian Endmembers for ambient (green) and UHV (red) conditions. (e−h) Corresponding Bayesian loading maps showing spatial distribution of intensity of each Endmember for ambient conditions. Adapted with permission from ref 40. Copyright American Chemical Society (2014). (i−k) Bayesian loading maps for UHV conditions.
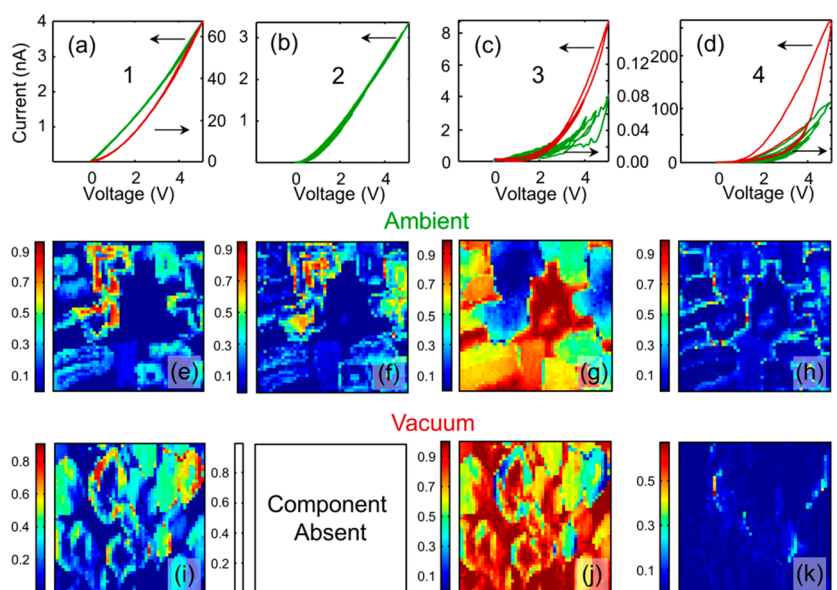

Figure 3. BLU of the FORC-IV data sets with maximal V_p = 5 V. (a−d) Bayesian Endmembers for ambient (green) and UHV (red) conditions. (e−h) Corresponding Bayesian loading maps for ambient conditions. (i−k) Bayesian loading maps for UHV conditions.

combination of position-independent endmembers, M, with respective relative abundances, A, corrupted by additive Gaussian noise N. The advantage of this method relies upon non-negativity ($M_i \geq 0$, $A_i \geq 0$), full additivity and sum-to-one ($\sum A_i = 1$) constraints for both the endmembers[49,50] and the abundance[51,52] coefficients, making it an ideal statistical vehicle for interpretation of physical behavior. Here the BLU algorithm was supplemented with an additional constraint requiring the difference between the reverse and forward branches of the endmembers be smaller than the default tolerance. This prevented splitting of nonhysteretic *IV* curves into a linear

combination of two endmembers with clockwise and counter-clockwise loop openings (see Methods for details).

The BLU algorithm estimates the initial projection of endmembers in a dimensionality reduced subspace (PCA) via N-FINDR,[53] a geometrical method that searches for a simplex of maximum volume that can be inscribed within the hyperspectral data set using a simple nonlinear inversion. The endmember abundance priors as well as noise variance priors are chosen by a multivariate Gaussian distribution, where the posterior distribution is calculated based on endmember independence using Markov Chain Monte Carlo that generates asymptotically distributed samples probed by Gibbs sampling

C

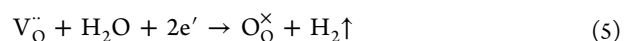strategy. Because of non-negativity of the resulting endmembers M and normalization of abundances, the spectrum at each location is decomposed into a linear combination of spectra of individual components in corresponding proportions. As the geometry of our sample implies a parallel combination of conduction channels (Figure 1e) with the total current at each location being a linear combination (sum) of the currents flowing through each channel, the latter can be represented by endmembers. The loading (abundance) maps then reflect the spatial distribution of intensities of each component. A more detailed description of the BLU method and degree of its applicability can be found elsewhere.[40]

The use of BLU method does not require a priori knowledge of pure spectra or number of components, although the later must be provided by the researcher. Estimation of the number of components k can be done using statistical methods (PCA, k-means, dendrogram construction) or by oversampling and undersampling the BLU k-values while analyzing the underlying physics until an optimum is found. In agreement with previous studies,[40] the optimal number of components for the system in ambient conditions with maximal V_p = 3 V is k = 4. Increasing the V_p to 5 V somewhat alters the conductive pattern but optimal k remains the same (see Supporting Information). The four distinct components for V_p = 3 V, V_p = 5 V, ambient, and UHV conditions are shown in Figures 2 and 3. The first component is characterized by a linear or almost linear nonhysteretic IV and is active in the inner part of the BFO–CFO interface (Figures 2 and 3a,e,i) . Component 2 (Figures 2b,f, j and 3b,f) shows a nonlinear nonhysteretic behavior and is most prominent at the core of the CFO islands and the outer part of the interface (at 5 V). The BFO matrix is highlighted by the third component (Figures 2 and 3c,g,k), displaying a 2 orders of magnitude lower conductivity than the other components. Finally, component 4 is highly nonlinear, hysteretic, and is confined to the outskirts of the interfaces (Figures 2d,h and 3d,h,k). Its spatial distribution extends further from the interface as V_p increases from 3 to 5 V. The optimal number of behaviors decreases by one for the data sets recorded in UHV and comparison of the resultant loading maps and endmembers with those of the ambient data sets allowed us to determine which components deactivate. Figures 2 and 3 present a thorough comparison of all four data sets. As can be seen, component 1 (Figures 2 and 3a,e,i) remains active in the inner part of the interface but is no longer fully linear. Component 4 (Figures 2 and 3d,h) disappears in UHV at max V_p = 3 V but appears again as a weak specter at max V_p = 5 V (Figure 3k). The hysteretic nature of this component must be due to electrochemical reactions taking place at the tip–surface junction and counter-reactions that can proceed at the bottom electrode or any virtual electrode.[54,55] However, the measured current is due to electronic transport, coupled to electrochemistry, rather than ionic transport per se, as concentration of oxygen vacancies in complex oxides is too low to sustain a measurable ionic current (see estimates in ref 8). The IV hysteresis or the difference between the conductivity during the forward and reverse voltage sweeps is similar to the resistive switching in memristive materials where electrochemical–electronic coupling exists. Electrochemical processes change the local concentration of oxygen vacancies (that act as electron donors) and thus influence the local position of the Fermi level controlling the local electronic transport. Other charged crystal defects will affect transport via similar mechanisms. In ambient, the positively charged tip can oxidize either lattice oxygen or

adsorbed water according to eqs 1 and 2 as expressed by the Kröger–Vink notation

$$2O_O^\times - 4e' \rightarrow 2V_O^{\cdot\cdot} + O_2\uparrow \tag{1}$$

$$4O_O^\times + 2H_2O - 4e' \rightarrow 4OH_O^\cdot + O_2\uparrow \tag{2}$$
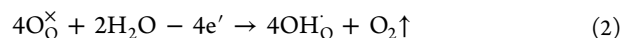
The first reaction effectively increases the local oxygen vacancy concentration, and the second injects protons into the lattice. Both of the defect effectively act like electron donors. The counter-reaction can be reduction of Fe^{3+}, oxygen or water as in eqs 3–5

$$Fe_{Fe}^\times + e' \rightarrow Fe_{Fe}' \tag{3}$$

$$2V_O^{\cdot\cdot} + O_2 + 4e' \rightarrow 2O_O^\times \tag{4}$$

$$V_O^{\cdot\cdot} + H_2O + 2e' \rightarrow O_O^\times + H_2\uparrow \tag{5}$$

To establish the rate limiting process, we note that the conductive behavior of the nanocomposite is dependent on the relative humidity (RH) of air (at 1 atm) with overall current increasing and threshold voltage decreasing in the range 0–87% RH.[47] Next, according to Le Chatelier principle, reaction in eq 1 would require less activation if p_{O_2} decreased (i.e., transferring the sample from ambient to vacuum), whereas reaction in eq 4, au contraire, would require an increase in thermodynamic force (in this case–voltage) for activation. Likewise, the threshold voltage for reaction in eq 2 depends inversely on the partial water pressure: $V_{th} = \text{Const} - \text{Const}' \cdot \log(p_{H_2O})$, which is in line with the fact that the electrochemical component 4 (Figures 2d,h and 3d,h,k) does not disappear altogether in UHV conditions but simply requires a higher voltage for activation. Thus, it is more likely that the process in eq 2 is in control of the overall transport behavior. It is the only process of the shown equations that has the same dependence on partial oxygen and water pressure as observed in the experiment. We shall return to this discussion in more details below, when comparing fitting of the fourth endmember to physical models. The reader should note here that the counter-reactions can hardly be the rate-limiting process, as at least one of them eq 3 is independent of the ambient gas and can proceed in UHV at the same rate as in ambient. Because the counter electrode is much larger than the tip–surface junction, a continuous electrochemical process on its surface is not current limiting.

Components 2 and 3 (Figures 2b,c,f,g,j,k and 3b,c,f,g,j) illustrate a more complex behavior in switching from ambient to UHV. At max V_p = 3 V both are present in same locations as in ambient, although the BFO component is characterized by very low current dominated by the circuit capacitance, rather than noise, as in ambient case. As the maximal peak bias increases to V_p = 5 V, however, the components merge together and BFO matrix shows conductive behavior similar to the core of the CFO islands.

Further insights into the conductive modality of the nanocomposite is gained by applying physical models to the behaviors extracted from the multidimensional data sets. The local electronic transport through the nanocomposite can be limited by either the electrode's surface junction, conductance of the bulk, or a combination of the two. The possible transport mechanisms, typical of electronic conductance in complex oxides are listed in Table 1. Application of these equations[18,56,57] to our tip–nanocomposite–bottom electrode system requires some modifications, as they were derived for a semiconductor in a uniform electric field. Therefore, for the

Table 1. Possible Transport Mechanisms in BFO−CFO Nanocomposite[a]

Fowler-Nordheim tunneling

$$I = S_{eff} \cdot \frac{q^3 m_{Pt}}{8\pi h m^* \varphi_B} E_{max}^2 \cdot e^{-\sqrt{\frac{128\pi^2 m^* \cdot q^2}{9h^2 q^2 \cdot E_{max}} \varphi_B^3}}$$

Schottky emission

$$I = S_{eff} \cdot A^{**} T^2 \cdot e^{-q\varphi_{B0}/kT} \cdot e^{+q/kT\left(\sqrt{\frac{qE_{max}}{4\pi\varepsilon_s}}\right)}$$

Poole-Frenkel conduction

$$I = S_{eff} \cdot q\mu n E_{bulk} \cdot e^{\left[-\frac{q}{kT}\left(\varphi_B - \sqrt{\frac{qE_{bulk}}{\pi\varepsilon_s}}\right)\right]}$$

Mott-Gurney Law

$$I = S_{eff} \cdot \frac{9\varepsilon\mu}{8d} E_{bulk}^2$$

Child's Law

$$I = S_{eff} \cdot \frac{4\varepsilon}{9} \sqrt{\frac{2q}{m^* d}} E_{bulk}^3$$

[a] S_{eff} is the effective tip−surface area; q is the elementary charge; m_{Pt} and m^* are effective electron masses in Pt and semiconductor; h is Planck's constant, ϕ_B is the barrier height; E_{max} is the maximal electric field in the metal−semiconductor interface; A^{**} is the effective Richardson constant; T is temperature; k is the Boltzmann constant; ε_s is the effective semiconductor permittivity; μ is the electron mobility in semiconductor; N_D is the dopant concentration; n is density of states in the conduction band; E_{bulk} is the electric field in the semiconductor bulk; and d is the sample thickness.

cases of Fowler−Nordheim and Schottky emission mechanisms, we assume abrupt junction approximation,[56] when the maximal electric field in the tip−surface junction is given by $E_{max} = ((2qN_D/\varepsilon_s)(V + V_{bi}))^{1/2}$; here V is the applied bias and V_{bi} is the built-in potential due to the difference between the metal and semiconductor work functions. For the cases of Poole−Frenkel and space-charge limited bulk conductance, we note that the local conductivity will strongly depend on the strength of the electric field, and therefore, current will be limited by the resistivity of the deep layers of the film, lying close to the bottom electrode, where electric field is the weakest and is proportional to the tip bias: $E_{bulk} = \alpha \cdot V/d$. Finite element modeling shows that the field enhancement factor α is on the order of 10.

Endmember fitting to the listed transport mechanisms can be ambiguous with some experimental data being equally well described by several different equations. We resolve this ambiguity by considering the physical validity of the parameters extracted by fitting. Thus, although some endmembers are fitted well to equations of the space-charge limited conductance mechanisms (Mott Gurney and Child's Laws), the extracted

effective electron masses and mobilities significantly diverge from expected values. We reported earlier[40] that for ambient conditions endmembers 2 and 3, (Figures 2b,c,f,g,j,k and 3b,c,f,g,j) as well as the forward branches of endmember 4 (Figures 2 and 3d), can be fitted to the FN mechanism, which yielded a potential barrier of 0.3−0.5 meV. These values are very low and are hard to justify physically. Moreover, the concentration of donor impurities calculated from these fits is also extremely low (on the order of 10^9-10^{11} cm^{-3}) whereas concentration of oxygen vacancies in complex oxides is expected to be in the range $10^{17}-10^{20}$ cm^{-3}. However, it follows that Bayesian endmembers can be equally well fitted to the reverse-biased Schottky barrier emission equation (which could be the case for the positive tip bias—see bipolar IV curves in ref 44). These fits yield barrier heights of 0.4−0.7 eV and donor concentrations in the expected range, which is consistent with the earlier reports.[42,58] Sorting through the possibilities, we note that all of the observed conductive behavior in both ambient and UHV can be described by two mechanisms: Ohmic conductance and Schottky emission. The former mechanism is evident from endmember 1 (Figures 2 and 3a) in the ambient data sets. The Schottky mechanism is apparently active in all other cases, except for endmember 3 (Figures 2 and 3b,c) of the UHV data set with maximal $V_p = 3$ V. These two mechanisms allow extraction of different parameters from the data, such as the material's conductivity from Ohmic conductance and potential barrier with donor concentration from the Schottky emission. In order to track changes in these parameters across the applied voltage and oxygen pressure ranges, we have fitted all of the endmembers to the aforementioned mechanisms and present them in Table 2 even if the fit was poor. This allows us to approximately compare dissimilar behaviors in terms of conductivity, potential barrier, and donor concentration.

The major trends of behavioral evolution are described below. First, probing the nanocomposite with a waveform of a higher maximal V_p increases the complexity of conductive behaviors. Whereas in ambient conditions at $V_p = 3$ V endmember 1 (Figure 2a) is perfectly linear, at $V_p = 5$ V it is slightly curved (Figure 3a). In UHV higher V_p leads to activation of the fourth endmember (Figure 3d) and consolidation of endmembers 2 and 3 (Figure 3c,j). Second, decreasing the partial oxygen pressure brings about a significant increase in conductivity (ca. 2-fold for averaged data and 10−

Table 2. Transport Parameters of the BFO−CFO Nanocomposite Extracted by Fitting

			En1	En2	En3	En4 FW	En4 RV
ambient	3 V	φ_B, eV	0.43[a]	0.53	0.71	0.71−0.63[b]	0.66−0.58[b]
		N_D, cm^{-3}	4×10^{17a}	35×10^{17}	59×10^{19}	$2.7-1.2 \times 10^{19b}$	$1.3-0.7 \times 10^{19b}$
		σ, mS/m	39	60[a]	1[a]	maximum 30[a]	
	5 V	φ_B, eV	0.46[a]	0.42	0.56	0.81−0.63[b]	0.64−0.56[b]
		N_D, cm^{-3}	9×10^{17a}	3×10^{17}	4×10^{19}	$5.0-1.0 \times 10^{19b}$	$1.0-0.4 \times 10^{19b}$
		σ, mS/m	45	60[a]	3[a]	maximum 60[a]	
UHV	3 V	φ_B, eV	0.42	0.53			
		N_D, cm^{-3}	16×10^{17}	80×10^{17}			
		σ, mS/m	700[a]	470[a]	5[a]		
	5 V	φ_B, eV	0.42		0.60	0.63−0.56[b]	0.55−0.51[b]
		N_D, cm^{-3}	17×10^{17}		1 and 73×10^{19c}	$3.3-1.5 \times 10^{19b}$	$1.2-1.1 \times 10^{19b}$
		σ, mS/m	1300[a]		260[a]	maximum 6400[a]	

[a] Indicates parameters extracted from a poor fit. [b] The range is from parameter at low voltage to high voltage parameter. [c] For CFO and BFO, respectively.

100-fold for individual endmembers), an increase in donor concentration (ca. 2-fold) and a very slight decrease in potential barrier (by 0.01−0.03 eV). Third, the fourth endmember tracks the resistive switching process at the BFO−CFO interface. The gradual increase in conductivity from cycle to cycle is evident from the dissimilarity of the forward (FW) and reverse (RV) branches of FORC-IV curves, the latter showing enhanced conductivity. As discussed above, this endmember is likely controlled by electrochemistry at the tip−surface junction. Table 2 summarizes the Schottky mechanism parameter change for the fourth endmember: both the donor (oxygen vacancy) concentration and potential barrier decrease with increasing voltage for both forward and reverse FORC-IV curves. Moreover, final N_D (i.e., for reverse curve) in air is lower than in UHV, and the drop in N_D is larger in air; both potential barrier and the drop in potential barrier are higher at higher oxygen pressure. For instance, for forward IV curves at maximal $V_p = 5$ V, $\Delta\varphi_B = 0.18$ eV, $N_D^{lowV}/N_D^{highV} = \gamma = 5$ in air, and $\Delta\varphi_B = 0.07$ eV, $\gamma = 2.2$ for UHV. As explained above, the oxygen vacancy concentration in the vicinity of the tip is regulated by eq 1, which implies creation of oxygen vacancies during application of positive bias. However, the donor concentration found from fitted data, decreases during positive voltage application. Moreover, oxidative water splitting eq 2 has a lower activation energy and, thus, is more likely to proceed at the tip−surface junction. Hence, we propose the following mechanism incorporating all of the observations. In ambient conditions due to high oxygen and water pressures, concentration of oxygen vacancies in the regions of the fourth endmember activity is low, and the initial Schottky barrier is high. In UHV, the surface states depopulate, increasing the number of near-surface oxygen vacancies and decreasing potential barrier as compared to ambient. Application of positive bias in air easily initiates reaction eq 2 leads to replacement of oxygen vacancies with protons in the vicinity of the tip. The latter significantly decreases potential barrier height due to their positive charge but are not as potent electron donors as oxygen vacancies, and therefore an effective decrease of N_D is observed. In UHV conditions, the same process requires a higher voltage and advances much slower due to lower concentration of water on the surface. Hence, a smaller decrease in both N_D and φ_B as compared to ambient is observed.

Finally, it is of interest to compare transport behaviors described by dissimilar endmembers. The donor concentration, potential barrier, and conductivity decrease in the following order: N_D 3 > 4 > 2 > 1; φ_B 4 ≈ 3 > 2 ≈ 1; σ 4 > 1 ≈ 2 > 3, where numbers stand for the corresponding endmembers. Interestingly, conductivity of BFO eq 3 is lowest, even though donor concentration is highest, and potential barrier is comparable with that of other components. This implies that the mobility of charge carriers in BFO is significantly lower than in CFO. In addition, endmember 3 (Figure 2c) manifests a prominent capacitive behavior in UHV conditions, seen in a wide FORC-IV loop opening with the forward and reverse curves running almost parallel to each other and only meeting at origin and V_p. The difference between the forward and reverse curves is then given by $\Delta I = 2C \cdot |dV/dt|$, where C is the circuit capacitance and dV/dt is the rate of voltage sweep. Capacitance, calculated from UHV data sets at maximal $V_p = 3$ and 5 V is 0.8 and 1.0 nF, respectively. Because of its low value, it only influenced the shape of endmember 3 (Figure 2c), which has very low conductivity. It is noteworthy that for the

ambient data sets capacitance is negligible, presumably, because a different instrument was used for these measurements. Thus, the measured capacitance is likely to reside in the electronic circuitry of the vacuum machine, rather than the sample itself. Ultimately, endmembers 1 and 2 (Figures 2e,f,i,j and 3e,f,i), highlight the transport behavior of CFO are independent of electrochemistry (i.e., their σ, N_D, and φ_B are almost independent of voltage) and the difference between the two is mainly determined by the potential barrier.

In conclusion, we have conducted a comparative study of complex transport behavior in a BFO−CFO nanocomposite employing a combination of the FORC-IV technique and data mining analysis. The four transport components found via Bayesian linear unmixing show variation as a function of voltage and ambient conditions, and can be explained in the framework of the Schottky emission and Ohmic transport models. The linear IV curves at the CFO−BFO interface and exponential behavior at the CFO island cores show increased conductivity in UHV at low voltage, and the memristive behavior of the outer interface disappears completely in these conditions. At higher voltage, behaviors of the CFO cores and BFO matrix become all but indistinguishable and the memristive component reappears once again. The observed behavior is discussed in the light of electrochemical control of electron transport via changes in the local Schottky barrier and oxygen vacancy concentration due to water splitting reaction. We note that in the future work a more precise numerical calculation not based on the uniform field assumption would be required to fully unravel the transport mechanisms peculiarities.

From a wider perspective, we demonstrate an approach to solve the convolution problem in spectroscopic imaging of spatially inhomogeneous systems. The use of statistical methods allows establishing the relevant number of statistically significant behaviors and blindly umixing the multidimensional data sets into individual components, thus losslessly compressing them into 1D and 2D objects perceptible by the researcher. Most importantly, rational selection of data mining approaches compatible with physical constraints allows direct interpretation of the unmixed behaviors in the framework of the chosen physical model, thus distilling physical meaning out of raw data.

Methods. BFO−CFO nanocomposite film of 100 nm was grown on 30 nm $SrRuO_3$ (SRO) buffered $SrTiO_3$ (001) substrates by pulsed lased deposition technique. Growth was monitored in situ using high-pressure reflective high-energy electron diffraction. Electrical measurements (c-AFM and FORC-IV) in ambient were performed on Cypher AFM (Asylum Research); in UHV we have utilized a Variable Temperature Omicron AFM/STM with a base pressure of 1×10^{-10} Torr or better. Both instruments were equipped with a National Instruments data acquisition card controlled through custom-written Matlab/LabView software. Voltage bias was applied to a conductive Cr/Pt coated (Budget Sensors) AFM tip, and current was detected off of the bottom electrode (SRO) with a Femto amplifier (DLPCA-200). Matlab codes were used for data processing, statistical analysis, and fitting. The BLU algorithm was supplemented with an additional constraint requiring the difference between the reverse and forward branches of the endmembers be smaller than the default tolerance. This prevented splitting of nonhysteretic IV curves into a linear combination of two endmembers with clockwise and counterclockwise loop openings. The counterclockwise loop opening (En 4 in Figures 2 and 3) is physically meaningful but the clockwise loop opening implies that current

of the forward branch would saturate past some voltage. While not impossible in principle, such behavior is not seen in the raw data at individual locations and therefore was deemed to be a mathematical artifact of BLU and corrected by this additional constraint. Parameters for fitting were the following: effective contact area, 1257 nm^2 (AFM tip radius of 20 nm); relative permittivity of BFO and CFO 58[59] and 14,[60] respectively; effective Richardson constant equal to Richardson constant.

■ ASSOCIATED CONTENT

ⓢ Supporting Information

The Supporting Information is available free of charge on the ACS Publications website at DOI: 10.1021/acs.nanolett.5b02472.

Selection of the *k*-parameter algorithm. (PDF)

■ AUTHOR INFORMATION

Corresponding Author
*E-mail: strelcove@ornl.gov.

Notes
The authors declare no competing financial interest.

■ ACKNOWLEDGMENTS

■ REFERENCES

(1) Imada, M.; Fujimori, A.; Tokura, Y. *Rev. Mod. Phys.* **1998**, *70*, 1039.

(2) Dagotto, E. *Science* **2005**, *309*, 257.

(3) Pentcheva, R.; Pickett, W. E. *J. Phys.: Condens. Matter* **2010**, *22*, 043001.

(4) Jeong, D. S.; Thomas, R.; Katiyar, R. S.; Scott, J. F.; Kohlstedt, H.; Petraru, A.; Hwang, C. S. *Rep. Prog. Phys.* **2012**, *75*, 076502.

(5) Tsymbal, E. Y.; Kohlstedt, H. *Science* **2006**, *313*, 181.

(6) Ohtomo, A.; Hwang, H. Y. *Nature* **2004**, *427*, 423.

(7) Herranz, G.; Basletić, M.; Bibes, M.; Carrétéro, C.; Tafra, E.; Jacquet, E.; Bouzehouane, K.; Deranlot, C.; Hamzić, A.; Broto, J. M.; al, e. *Phys. Rev. Lett.* **2007**, *98*, 216803.

(8) Seidel, J.; Martin, L. W.; He, Q.; Zhan, Q.; Chu, Y. H.; Rother, A.; Hawkridge, M. E.; Maksymovych, P.; Yu, P.; Gajek, M.; et al. *Nat. Mater.* **2009**, *8*, 229.

(9) Maksymovych, P.; Seidel, J.; Chu, Y. H.; Wu, P. P.; Baddorf, A. P.; Chen, L. Q.; Kalinin, S. V.; Ramesh, R. *Nano Lett.* **2011**, *11*, 1906.

(10) Maksymovych, P.; Morozovska, A. N.; Yu, P.; Eliseev, E. A.; Chu, Y. H.; Ramesh, R.; Baddorf, A. P.; Kalinin, S. V. *Nano Lett.* **2012**, *12*, 209.

(11) Farokhipoor, S.; Noheda, B. *Phys. Rev. Lett.* **2011**, *107*, 127601.

(12) Guyonnet, J.; Gaponenko, I.; Gariglio, S.; Paruch, P. *Adv. Mater.* **2011**, *23*, 5377.

(13) Wu, W. D.; Horibe, Y.; Lee, N.; Cheong, S. W.; Guest, J. R. *Phys. Rev. Lett.* **2012**, *108*, 077203.

(14) Wu, W. D.; Guest, J. R.; Horibe, Y.; Park, S.; Choi, T.; Cheong, S. W.; Bode, M. *Phys. Rev. Lett.* **2010**, *104*, 217601.

(15) Maksymovych, P.; Jesse, S.; Yu, P.; Ramesh, R.; Baddorf, A. P.; Kalinin, S. V. *Science* **2009**, *324*, 1421.

(16) Garcia, V.; Fusil, S.; Bouzehouane, K.; Enouz-Vedrenne, S.; Mathur, N. D.; Barthelemy, A.; Bibes, M. *Nature* **2009**, *460*, 81.

(17) Gruverman, A.; Wu, D.; Lu, H.; Wang, Y.; Jang, H. W.; Folkman, C. M.; Zhuravlev, M. Y.; Felker, D.; Rzchowski, M.; Eom, C. B.; et al. *Nano Lett.* **2009**, *9*, 3539.

(18) Maksymovych, P.; Pan, M. H.; Yu, P.; Ramesh, R.; Baddorf, A. P.; Kalinin, S. V. *Nanotechnology* **2011**, *22*, 254031.

(19) Strelcov, E.; Lilach, Y.; Kolmakov, A. *Nano Lett.* **2009**, *9*, 2322.

(20) Nakano, M.; Shibuya, K.; Okuyama, D.; Hatano, T.; Ono, S.; Kawasaki, M.; Iwasa, Y.; Tokura, Y. *Nature* **2012**, *487*, 459.

(21) Hormoz, S.; Ramanathan, S. *Solid-State Electron.* **2010**, *54*, 654.

(22) Mannhart, J.; Schlom, D. G. *Science* **2010**, *327*, 1607.

(23) Sawa, A. *Mater. Today* **2008**, *11*, 28.

(24) Szot, K.; Rogala, M.; Speier, W.; Klusek, Z.; Besmehn, A.; Waser, R. *Nanotechnology* **2011**, *22*, 254001.

(25) Waser, R.; Dittmann, R.; Staikov, G.; Szot, K. *Adv. Mater.* **2009**, *21*, 2632.

(26) Strukov, D. B.; Snider, G. S.; Stewart, D. R.; Williams, R. S. *Nature* **2008**, *453*, 80.

(27) Wolkenstein, T. *Electronic Processes on Semiconductor Surfaces during Chemisorption*; Consultants Bureau: New York, 1991.

(28) Barsan, N.; Schweizer-Berberich, M.; Göpel, W. *Fresenius' J. Anal. Chem.* **1999**, *365*, 287.

(29) Gruverman, A. *J. Mater. Sci.* **2009**, *44*, 5182.

(30) Crassous, A.; Bernard, R.; Fusil, S.; Bouzehouane, K.; Briatico, J.; Bibes, M.; Barthélémy, A.; Villegas, J. E. *J. Appl. Phys.* **2013**, *113*.

(31) Kalinin, S. V.; Balke, N. *Adv. Mater.* **2010**, *22*, E193.

(32) Kalinin, S.; Balke, N.; Jesse, S.; Tselev, A.; Kumar, A.; Arruda, T. M.; Guo, S. L.; Proksch, R. *Mater. Today* **2011**, *14*, 548.

(33) Giridharagopal, R.; Shao, G. Z.; Groves, C.; Ginger, D. S. *Mater. Today* **2010**, *13*, 50.

(34) Gerber, C.; Lang, H. P. *Nat. Nanotechnol.* **2006**, *1*, 3.

(35) Bonnell, D. A.; Garra, J. *Rep. Prog. Phys.* **2008**, *71*, 044501.

(36) Belianinov, A.; Ganesh, P.; Lin, W.; Sales, B. C.; Sefat, A. S.; Jesse, S.; Pan, M.; Kalinin, S. V. *APL Mater.* **2014**, *2*, 120701.

(37) Vasudevan, R. K.; Belianinov, A.; Gianfrancesco, A. G.; Baddorf, A. P.; Tselev, A.; Kalinin, S. V.; Jesse, S. *Appl. Phys. Lett.* **2015**, *106*, 091601.

(38) Tselev, A.; Ivanov, I. N.; Lavrik, N. V.; Belianinov, A.; Jesse, S.; Mathews, J. P.; Mitchell, G. D.; Kalinin, S. V. *Fuel* **2014**, *126*, 32.

(39) Dobigeon, N.; Moussaoui, S.; Coulon, M.; Tourneret, J. Y.; Hero, A. O. *IEEE Transactions on Signal Processing* **2009**, *57*, 4355.

(40) Strelcov, E.; Belianinov, A.; Hsieh, Y.-H.; Jesse, S.; Baddorf, A. P.; Chu, Y.-H.; Kalinin, S. V. *ACS Nano* **2014**, *8*, 6449.

(41) Zavaliche, F.; Zhao, T.; Zheng, H.; Straub, F.; Cruz, M. P.; Yang, P. L.; Hao, D.; Ramesh, R. *Nano Lett.* **2007**, *7*, 1586.

(42) Hsieh, Y.-H.; Liou, J.-M.; Huang, B.-C.; Liang, C.-W.; He, Q.; Zhan, Q.; Chiu, Y.-P.; Chen, Y.-C.; Chu, Y.-H. *Adv. Mater.* **2012**, *24*, 4564.

(43) Aimon, N. M.; Kim, D. H.; Sun, X.; Ross, C. A. *ACS Appl. Mater. Interfaces* **2015**, *7*, 2263.

(44) Hsieh, Y.-H.; Strelcov, E.; Liou, J.-M.; Shen, C.-Y.; Chen, Y.-C.; Kalinin, S. V.; Chu, Y.-H. *ACS Nano* **2013**, *7*, 8627.

(45) Strelcov, E.; Kim, Y.; Jesse, S.; Cao, Y.; Ivanov, I. N.; Kravchenko, I. I.; Wang, C. H.; Teng, Y. C.; Chen, L. Q.; Chu, Y. H.; Kalinin, S. V. *Nano Lett.* **2013**, *13*, 3455.

(46) Kim, Y.; Strelcov, E.; Hwang, I. R.; Choi, T.; Park, B. H.; Jesse, S.; Kalinin, S. V. *Sci. Rep.* **2013**, *3*, 2924.

(47) Belianinov, A.; Vasudevan, R.; Strelcov, E.; Steed, C.; Yang, S.; Tselev, A.; Jesse, S.; Biegalski, M.; Shipman, G.; Symons, C.; Borisevich, A.; Archibald, R.; Kalinin, S. *Adv. Struct Chem. Imag* **2015**, *1*, 1.

(48) Dobigeon, N.; Moussaoui, S.; Coulon, M.; Tourneret, J. Y.; Hero, A. O. *Signal Processing, IEEE Transactions on* **2009**, *57*, 4355.

(49) Moussaoui, S.; Brie, D.; Mohammad-Djafari, A.; Carteret, C. *IEEE Trans. Signal Process.* **2006**, *54*, 4133.

(50) Dobigeon, N.; Moussaoui, S.; Tourneret, J. Y. *Proc. IEEE-SP Workshop Stat. and Signal Processing*; Madison, WI, 2007; p 79.

(51) Parra, L.; Mueller, K.-R.; Spence, C.; Ziehe, A.; Sajda, P. *Advances in Neural Information Processing Systems (NIPS) 12*; MIT Press: Cambridge, MA, 2000; p 942.

(52) Dobigeon, N.; Tourneret, J. Y.; Chein, I. C. *Signal Processing, IEEE Transactions on* **2008**, *56*, 2684.

(53) Winter, M. E. *Proc. SPIE* **1999**, *266*, 264.

(54) Arruda, T. M.; Kumar, A.; Kalinin, S. V.; Jesse, S. *Nano Lett.* **2011**, *11*, 4161.

(55) Yang, S. M.; Strelcov, E.; Paranthaman, M. P.; Tselev, A.; Noh, T. W.; Kalinin, S. V. *Nano Lett.* **2015**, *15*, 1062.

(56) Sze, S. M. *Physics of Semiconductor Devices*, 2nd ed.; John Wiley & Sons: New York, 1981.

(57) Chiu, F.-C. *Adv. Mater. Sci. Eng.* **2014**, 1.

(58) Clark, S. J.; Robertson, J. *Appl. Phys. Lett.* **2007**, *90*, 132903.

(59) Chen, W.-t.; Williams, A. J.; Ortega-San-Martin, L.; Li, M.; Sinclair, D. C.; Zhou, W.; Attfield, J. P. *Chem. Mater.* **2009**, *21*, 2085.

(60) Gutierrez, D.; Foerster, M.; Fina, I.; Fontcuberta, J.; Fritsch, D.; Ederer, C. *Phys. Rev. B* **2012**, *86*, 064117.